Hartmann-Shack wavefront sensing without a lenslet array using a digital micromirror device

BRIAN VOHNSEN,* ALESSANDRA CARMICHAEL MARTINS, SALIHAH QAYSI, AND NAJNIN SHARMIN

Advanced Optical Imaging Group, School of Physics, University College Dublin, Dublin 4, Ireland
**Corresponding author: brian.vohnsen@ucd.ie*

Received XX Month XXXX; revised XX Month, XXXX; accepted XX Month XXXX; posted XX Month XXXX (Doc. ID XXXXX); published XX Month XXXX

The common Hartmann-Shack wavefront sensor makes use of a lenslet array to sample in-parallel optical wavefronts. Here, we introduce a Hartmann-Shack wavefront sensor that employs a digital micromirror device in combination with a single lens for serial sampling by scanning. Sensing is analyzed numerically and validated experimentally using a deformable mirror operated in closed-loop adaptive optics with a conventional Hartmann-Shack wavefront sensor, as well as with a set of ophthalmic trial lenses, to generate controllable amounts of monochromatic aberrations. The new sensor is free of crosstalk and can potentially operate at kHz speed. It offers a reconfigurable aperture that can exclude unwanted parts of the wavefront. © 2018 Optical Society of America

OCIS codes: *(010.1080) Active or adaptive optics; (010.7350) Wave-front sensing; 220.1010 Aberrations (global); (200.6046) Smart pixel systems; (280.4788) Optical sensing and sensors.*

http://dx.doi.org/10.1364/AO.99.099999

1. INTRODUCTION

Quantification and correction of optical aberrations is essential in a wide range of applications including astronomy, free-space communications, lasers, microscopy and ophthalmology. Different methods have been developed to quantify aberrations including interferometry [1], Hartmann-Shack wavefront sensing (HS-WFS) and related methods [1-4], curvature sensing [5], pyramid wavefront sensing (P-WFS) [6,7], and quasi-resonant sensing using surface-plasmon polaritons (SPP-WFS) [8]. Some of these methods can be coded into liquid-crystal spatial light modulators (SLM) to allow real-time tuning of sensing parameters [3,7,9] although the resulting speed is typically limited to 10's of Hz. Relatedly, liquid-filled lenslet arrays have also been proposed allowing for increased flexibility when compared to conventional fixed lenslet arrays [10]. Digital micromirror devices (DMD) allow significantly higher modulation speed in the kHz range as binary elements. They have been used in applications that include retinal imaging [11], psychophysical vision testing [12], and lately also coded wavefront sensing [13].

Here, we propose the use of a fast DMD for wavefront sensing using a single-lens HS. Serial sensing is used to avoid the use of a lenslet array and thereby increase the dynamic range of the DMD-HS-WFS. Others have proposed an adaptive spot search method to extend the range of conventional HS-WFS [14] or phase retrieval using serial sensing with mechanical translation of a subaperture [15]. A large dynamic range can benefit ophthalmic applications including the determination of ocular aberrations [16] and adaptive optics (AO) retinal imaging [17] with special relevance for patients having eye disorders. The option of excluding unwanted corneal reflections with the switchable DMD array is highly attractive since such reflections can easily mask backscattered light from the retina. Like the conventional HS-WFS, a camera is used to capture the point-spread-function (PSF) although a rapid quadrant position detector could suffice to determine the PSF centre-of-gravity (CoG) at higher speed (>100 kHz). The small pixel size of the DMD allows for up to approximately 100×100-times denser sampling than a typical lenslet array. We discuss the principles of the sensor using numerical analysis in Matlab™ followed by an experimental proof-of-principle verification, discussion and conclusions.

2. EXPERIMENTAL SETUP

A schematic of the setup used for testing and verification of the DMD-HS-WFS is shown in Fig. 1. The DMD is a Vialux™ V-7001 VIS with 1024×768 diagonally hinged micromirrors and 13.7 μm pitch (92% fill factor) that can tilt independently -12° and +12°. The micromirrors allow redirecting reflected light at ±24° (optical angle) at a speed of 22.727 kHz. The DMD is used for serial scanning of the incident

wavefront such that only a small part is sampled at any instant in time. This light is focused onto a position sensitive detector, here a Thorlabs™ DCU223M CCD camera with ε = 4.65 μm pixel size. Thus, it operates as a conventional HS-WFS but with the parallel sensing lenslet array replaced by temporal sweeping of a reflective DMD cell that may consist of one or more adjacent micromirrors.

The light used is a spatially filtered and expanded beam from a HeNe laser (λ = 632.8 nm wavelength) truncated to a 3.0 mm diameter. A 140 actuator Boston Micromachines™ Multi-3.5 deformable mirror (DM) operated in closed-loop AO with a Thorlabs™ HS-WFS 150-5C is used to generate controllable amounts of Zernike aberrations across the beam of light. The truncation is necessary since the AO system can only manipulate the wavefront within the active area of the DM. A series of PSF images are captured with the CCD for each reflective DMD cell using an achromatic lens having f_L = 50 mm focal length. Two 4*f* telescopes with unit magnification using sets of 150 mm and 200 mm focal length achromatic lenses project the pupil plane from the DM to the DMD and to the entrance pupil of the CCD detector. This gives a direct relation between the sampled wavefront and the position of the PSF. Thus, when no aberrations are present all PSF images will be centred (reference images) and aberrations will translate the position of the PSF images in the same way as a conventional HS-WFS with a lenslet array. An iris with an 8 mm large opening (to avoid truncation) is used to block unwanted light (-24°) from the DMD whereby only the binary sampled part of the beam (+24°) is captured at any instant.

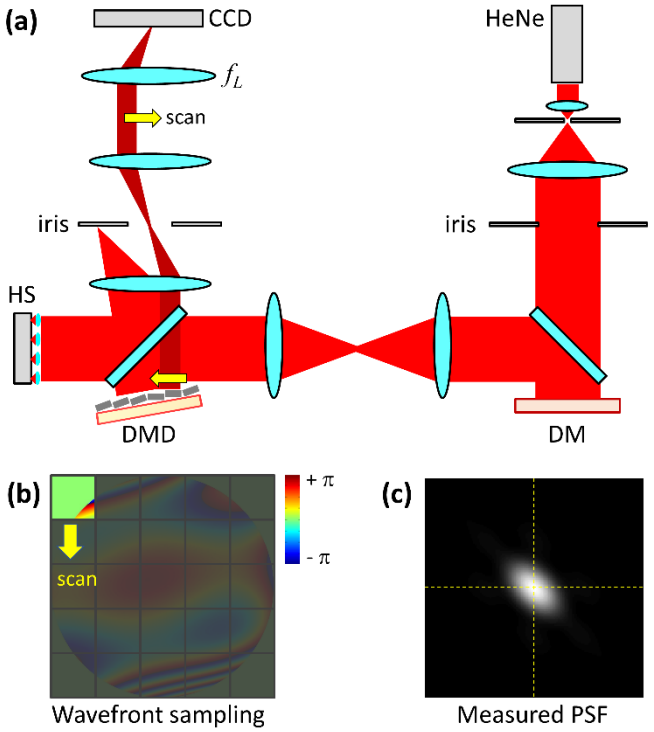

Fig. 1. (a) Schematic of the system used to verify the operation of the DMD-HS-WFS with serial scanning of a reflective DMD cell consisting of one or many adjacent micromirrors; (b) raster scanning of the wavefront (phase wrapped onto -π to +π) with the DMD cell; (c) CoG determination of the PSF for each sequentially active DMD cell. The DMD is tilted horizontally and vertically to compensate the 24° reflection angle. All lenses are antireflection-coated achromatic doublets.

3. NUMERICAL MODEL

To verify the operation of the method, simulated DMD cell raster scans have been performed with adjustable parameters prior to the experimental realization. Thus, wavefront aberrations are introduced across the incident beam as individual or linear combinations of Zernike polynomials Z_i. Only DMD cells where the illumination covers at least 50% of their area are included to ensure that focal spots are not significantly altered by uneven illumination, such as the partially illuminated cell at the rim of the beam shown in Fig. 1(b), which is more prone to diffraction and lower signal-to-noise ratio in the captured PSF.

The wavefront aberration in the pupil plane Φ_{WA} is expressed using polar coordinates (r,θ) and a series expansion including up to the 4th Zernike radial order as

$$\Phi_{WA}(r,\theta) = k\sum_i c_i Z_i(r,\theta) \tag{1}$$

where $k = \dfrac{2\pi}{\lambda}$ is the wave number and c_i are Zernike coefficients. The PSF is captured with the detector (CCD) for each position of the sampling DMD cell of size $w \times w$ scanned across the beam. Thus, the sampled PSF in cartesian coordinates $(\tilde{x},\tilde{y})$ is related to the wavefront aberration at the pupil via a Fourier Transform (FT) as

$$\mathrm{PSF}(\tilde{x},\tilde{y}) \propto \left|\mathrm{FT}\left\{\mathrm{rect}\left(\frac{x-x_0}{w}\right)\mathrm{rect}\left(\frac{y-y_0}{w}\right)P(x,y)\exp\left(i\Phi_{WA}(x,y)\right)\right\}\right|^2 \tag{2}$$

for an active DMD cell centred at (x_0,y_0). The rect function equals unity within each cell and zero outside of it. The profile of the beam is described by the pupil function P which here equals 1 inside and 0 outside of it, but it can easily account for the actual intensity profile too. Due to the high filling factor of the DMD, diffraction by the micromirror pitch has been omitted in Eq. (2). It produces weak diffraction orders at ±2.65° (and beyond) corresponding to a 9.2 mm shift at the lens and is effectively blocked by the iris. It can be included in the calculation by subdividing each DMD cell into an array of rect functions representative of the active micromirrors but for simplicity this will not be done here.

Eq. (2) can be expressed using convolutions * of sinc functions as

$$\begin{aligned}\mathrm{PSF}(\tilde{x},\tilde{y}) \propto \\ \left|\exp\left(-i2\pi f_x x_0\right)\mathrm{sinc}\left(\pi f_x w\right) * \right. \\ \exp\left(-i2\pi f_y y_0\right)\mathrm{sinc}\left(\pi f_y w\right) * \\ \left.\mathrm{FT}\left\{P(x,y)\exp\left(i\Phi_{WA}(x,y)\right)\right\}\right|^2 .\end{aligned} \tag{3}$$

where the spatial frequencies $f_x = \dfrac{\tilde{x}}{\lambda f_L}$, $f_y = \dfrac{\tilde{y}}{\lambda f_L}$ are determined by the imaging lens f_L and the CCD coordinates. The peak of the sinc functions are centered at the origin and are narrowest when w is large. In turn, when w is small (such as when the DMD cell consists of a single

micromirror at a time) the spatial width of the sinc functions widens. If $w = \frac{2\lambda f_L}{\varepsilon}$, which for the chosen system parameters corresponds to 13 mm, the peak of the sinc functions would be confined to a single CCD pixel. When chosen smaller, the peak spreads across more pixels. In this study w = 0.6 mm and w = 0.3 mm have been chosen to spread the sampled PSF across the central pixels of the CCD. The same relation can also be used to optimize sensing with a quadrant detector of a given size.

The raster scanning via the coordinates (x_0, y_0) modifies sequentially the DMD phase factors in Eq. (3) thereby sampling the PSF. If the wavefront is planar with a tilt $\theta_{\tilde{x}}$ in the $\tilde{x}$ direction, it produces a translation $\Delta\tilde{x} = f_L \sin(\theta_{\tilde{x}}) \approx f_L \theta_{\tilde{x}}$ of the PSF due to the shift theorem of the FT and a spot width set by the convolution in Eq. (3). The small-angle approximation of the sin function is valid for all angles considered in this study due to the small size of the CCD sensor with respect to the focal length of the imaging lens. In general, aberrations will shift the CoG of the sampled PSF. When w is small this will be encoded as a local tip/tilt in the same way as when using dense lenslets with a conventional HS-WFS. Indeed, Eq. (2) and Eq. (3) can easily be modified to describe a HS-WFS using a lenslet array by including a lens phase transfer function with each rect function.

The PSF is recorded for each position of the DMD cell and for centroiding the CoG coordinates $(\tilde{x}_c, \tilde{y}_c)$ are calculated as

$$\tilde{x}_c = \frac{\sum_{m,n} \tilde{x}_{m,n} I_{m,n}}{\sum_{m,n} I_{m,n}} ; \tilde{y}_c = \frac{\sum_{m,n} \tilde{y}_{m,n} I_{m,n}}{\sum_{m,n} I_{m,n}} \quad (4)$$

where $\tilde{x}_{m,n}$ and $\tilde{y}_{m,n}$ refer to individual CCD pixels (m,n) of intensity $I_{m,n}$. More advanced centroiding methods could be used to reduce the impact of noise or to adapt the CoG estimation to, for example, a region of interest on the CCD with fewer pixels, a quadrant detector, and a noise floor cutoff.

The least-square-estimate of the reconstructed Zernike coefficients c^{est} is determined as

$$c^{est} = \left[\boldsymbol{A}^T \boldsymbol{A}\right]^{-1} \boldsymbol{A}^T b^{meas} \quad (5)$$

where $\boldsymbol{A}$ is a tensor of Zernike polynomial derivatives, $\boldsymbol{A}^T$ is the transpose of $\boldsymbol{A}$, and $\left[\boldsymbol{A}^T \boldsymbol{A}\right]^{-1} \boldsymbol{A}^T$ is its pseudoinverse. The vector b^{meas} consists of measured wavefront slopes determined by the translation coordinates of each PSF CoG with respect to that obtained using a planar reference wave. Other wavefront reconstruction methods are readily available both in terms of computing Zernike coefficients and in terms of direct reconstruction from the centroid displacement without a projection onto Zernike modes [18]. However, since the control loop of the AO system used operates directly with Zernike coefficients, and since Zernike coefficients are of special relevance for ophthalmic applications., this approach was chosen for the study.

Simulated sensing and reconstruction of individual Zernike polynomials arranged according to the ANSI Z80.28-2010 standard are shown in Fig. 2 for two different DMD sampling densities. The quality of the simulated reconstruction in terms of the root-mean-square (RMS) Zernike reconstruction $\mathrm{RMS} = \sum_i |c_i|^2$ is very high for low-order aberrations and deteriorates only slightly with increasing aberration order. When using 10×10 DMD cells (1 cell equals 22×22 individual micromirrors) the reconstruction is practically identical to the incident wavefront. For the 5×5 DMD cells (1 cell equals 44×44 individual micromirrors) a slight deterioration can be seen such as an imperfect rotational symmetry for spherical aberration (Z_{13}).

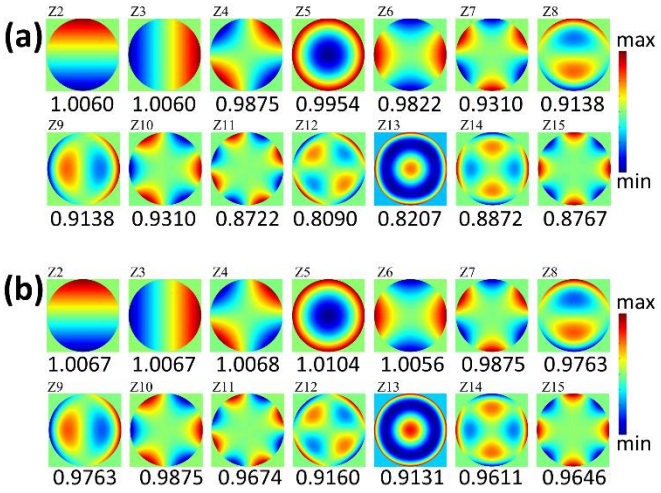

Fig. 2. Numerical simulation of DMD-HS-WFS of individual Zernike polynomials (excluding piston) with coefficients of 1 μm each scaled to the full scalebar using (a) 5×5 DMD cell (each 600×600 μm²) swept across the beam producing 25 sampled PSF's; (b) 10×10 DMD cell (each 300×300 μm²) producing 100 sampled PSF's. The magnitude of the reconstructed wavefront RMS (in μm units) is shown below each map. Only PSF's from DMD cells that are illuminated across more than 50% of their entire aperture have been included in the reconstruction.

The diagram in Fig. 3 shows a comparison of the reconstruction when the incident illumination area covers at least 50% of each contributing DMD cell and the situation where only cells covered by 100% have been included to avoid beam truncation.

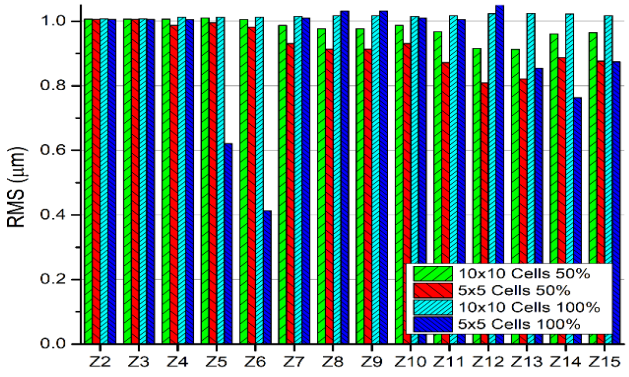

Fig. 3. Comparison of simulated sensing and reconstruction of individual Zernike polynomials with 1 μm coefficients with the DMD-HS-WFS using 5×5 and 10×10 DMD cells and with inclusion of all 100% illuminated cells and those covered by at least 50%., respectively.

As can be seen, when only fully illuminated cells are included, the obtained RMS is closest to the expected with 10×10 cells. However, with 5×5 cells a significant reduction in quality can be observed for some coefficients as this corresponds to just the central 3×3 cells in Fig. 1. Denser DMD sampling follows the beam periphery more closely and is therefore less affected.

Fig. 4 show simulations with reconstruction of random aberrations of increasing RMS wavefront error (same aberration with scaled Zernike coefficients) including only DMD cells that are fully illuminated. Again, it can be noted that the low sampling density provides a fair approximation, but the denser sampling captures more details.

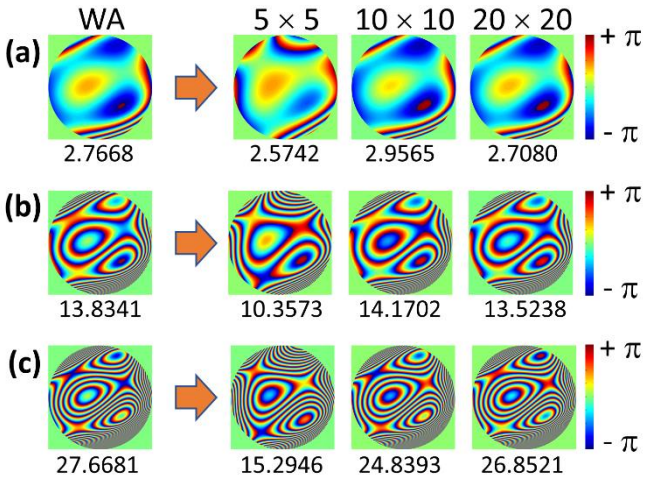

Fig. 4. Numerical simulation of DMD-HS-WFS reconstruction of a linear combination of Zernike polynomials with random coefficients in the range 0 – 1 μm scaled with (a) ×1 (RMS 2.7668 μm); (b) ×5 (RMS 13.8341 μm); and (c) ×10 (RMS 27.6681 μm). Reconstruction with DMD swept cells of 5×5 (each 600×600 μm²); 10×10 (each 300×300 μm²); 20×20 (each 150×150 μm²) are shown. The magnitude of the reconstructed wavefront RMS (in μm units) is shown below each map (phase wrapped onto -π to +π).

Fig. 4 also shows that the dynamic range of the sensor can, in principle, be very large. The reason is that there is no PSF crosstalk which limits the range of the conventional HS-WFS. The dynamic range is set by the *f*-number of the optics used to project the active DMD cell onto the detector (CCD) and the 24° reflection angle used to separate the sampled wavefront from the rest of the light at any instant.

4. EXPERIMENTAL RESULTS

An experimental verification was done with the system shown in Fig. 1. The results using a 5×5 DMD cell swept across the beam are shown in Fig. 5 for the same Zernike polynomials as shown in Fig. 2. The AO system consisting of the DM and HS-WFS was set to generate the individual Zernike modes. The DMD was raster scanned by software and images were captured manually (at low speed). The limited stroke of the DM prevents the AO system from reaching the full Zernike coefficients for high-order modes. For comparison, the system was set to generate both positive and negative Zernike coefficients, i.e., ±1 μm that were sensed with the DMD-HS-WFS and reconstructed with respect to a planar reference wave. Some asymmetry can be noticed caused by a slight offset in the DMD alignment with respect to the pupil of the AO system. This could be overcome either by pixelwise alignment of the DMD (it was aligned by visual inspection of the reflected light with circular projection images) or by postprocessing of the reconstruction pupil. The tilt of the DMD causes a slight deviation for the cartesian coordinates used which could be corrected using a rotated reference system [19]. Despite of the tilt, the large focal length of the telescopes ensures that the DMD is approximately conjugated to the pupil across the beam.

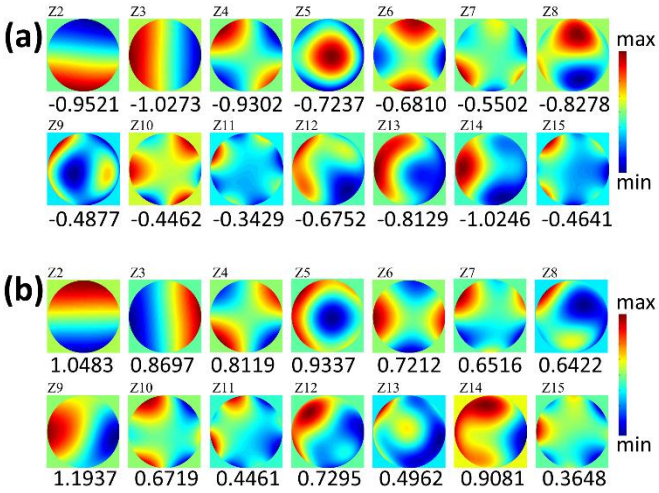

Fig. 5. Experimental verification of the DMD-HS-WFS of individual Zernike polynomials (excluding piston) each scaled to the full scalebar and generated with the AO system with coefficients of (a) -1 μm and (b) +1 μm and sensed using 5×5 DMD (each 600×600 μm²) swept cells across the beam producing 25 sampled PSF's. Only PSF's from DMD cells that are illuminated across at least 50% of their apertures have been included in the reconstruction. The magnitude of the reconstructed wavefront RMS (in μm units) is shown below each map.

For comparison, reconstruction was also made when including only DMD cells that are fully illuminated. The results of this are shown in Fig. 6.

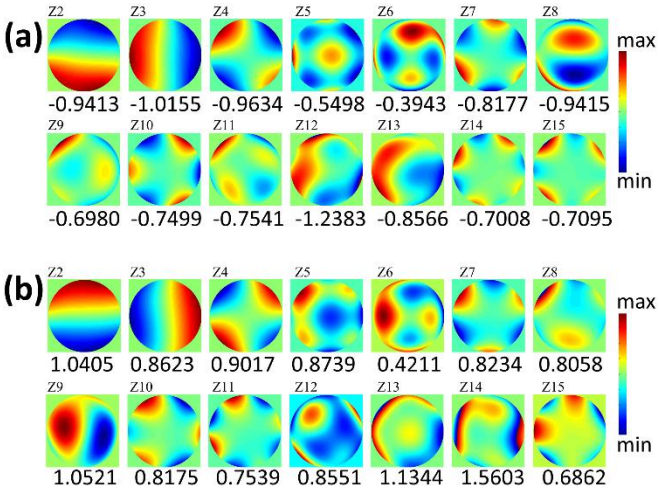

Fig. 6. Experimental verification of the DMD-HS-WFS of individual Zernike polynomials (excluding piston) each scaled to the full scalebar and generated with the AO system with coefficients of (a) -1 μm and (b) +1 μm and sensed using 5×5 DMD (each 600×600 μm²) swept cells across the beam producing 25 sampled PSF's. Only PSF's from DMD

cells that are fully illuminated across their entire apertures have been included in the reconstruction. The magnitude of the reconstructed wavefront RMS (in μm units) is shown below each map.

As expected, some of the Zernike modes are reconstructed with higher accuracy when using only fully illuminated cells. The lack of stroke of the DM used is noticeable in the reconstruction of the higher-order modes as can be seen in the RMS values shown below each image map that fall short of the requested ±1 μm.

To verify the large dynamic range of the DMD-HS-WFS, a set of tests without the limited-stroke AO system but with a set of ophthalmic trial lenses was used to generate defocus. Fig. 7 shows the measurement results for these cases. The reconstruction is approximately linear in the range of -5D to +5D (R-squared of 0.9971) although the determined c_5 coefficients shown below each image map in Fig. 7 differ somewhat from the expected values of ±0.33, ±1.62 and ±3.25 μm calculated for a 3.0 mm beam using the dioptric powers quoted by the lens manufacturer (MSD™).

It gradually fails as the size of the PSF on the camera becomes very large and the CoG expressed by Eq. (4) less accurate. This could be improved with better centroiding methods [20-22] or with a sensor having higher bit depth than the 8-bit CCD used which is prone to saturation. Indeed, the potential large dynamic range can be appreciated from the simulation in Fig. 4 with even a low sampling density. This was also verified numerically with defocus up to $c_5 = \pm 1000$ μm (not shown here).

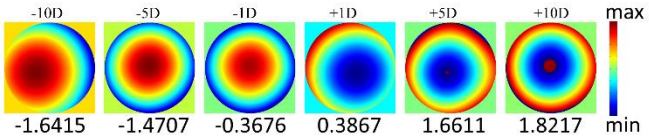

Fig. 7. Experimental verification of the DMD-HS-WFS reconstructing defocus generated by ophthalmic trial lenses in place of the AO system using from -10 to +10 diopters. All maps have been adjusted individually to the full scalebar that include 2π phase wrapping when the defocus is largest. The wavefront was determined by use of a 5×5 DMD cell (each 600×600 μm^2) swept across the beam producing a total of 25 sampled PSF's. Only PSF's from DMD cells that are illuminated across at least 50% of their apertures have been included in the reconstruction. The number below each map show the reconstructed Zernike defocus coefficient, c_5 expressed in μm units.

5. DISCUSSION

The serial wavefront sensing with the DMD-HS-WFS rather than parallel sampling of the entire wavefront as with a conventional HS-WFS solves the problem of crosstalk between adjacent focal points since only one PSF is sampled at any instant in time. The analysis in Fig. 4 and Fig. 7 demonstrate the potential of the sensor for large aberrations. The reconstructed Zernike defocus coefficients up to ±5D are in fair agreement with the expectations. Differences may relate to inaccuracies in the ophthalmic trial lenses and the wavelength used, mounting and centration inaccuracies, or edge diffraction by the truncation of the input beam. The DMD could be used to truncate the beam rather than the iris but this would increase straylight. Also, a current-tuneable lens or a larger-stroke DM could be used to vary the amount of defocus induced to eliminate the variation caused by mounting errors of the trial lenses.

The use of a fast centroiding method with a quadrant detector [21] or binary phase modulation [23] could allow high-speed wavefront sensing. The potential speed limit with different DMD cell sampling densities is shown in Table 1. The higher speed offered by binning of micromirrors in larger DMD cells may allow tracking of rapid aberration changes as well as oversampling by partially overlap of the DMD raster scan cells. Other methods than the simple CoG used here could be used to determine the most appropriate centroiding algorithm for a given application to increase speed and accuracy. Truncation and noise would become relevant in low-light applications requiring, for example, intensity-weighted noise suppression or an iterative determination [21,22].

Table 1. Scanning speed limit for a 22.727 kHz DMD. *If using two detectors with both the +24° and -24° reflection angles the indicated limit could double.

DMD cells	5×5	10×10	20×20	768×768
Sensing limit*	909 Hz	227 Hz	57 Hz	0.039 Hz

The possible dense sampling of the wavefront at intervals given by the DMD pixel pitch may prove useful for extreme adaptive optics [24], branching at phase singularities [25] or lithography [26]. Speed may be a limiting factor although faster DMD's (at 32 kHz) are becoming available. The size of the detected PSF is inversely proportional to the DMD cell size and thus detector noise and DMD diffraction may become an issue at very high sampling densities. A more compact system would be required to limit the width of the captured PSF's. A larger reflection angle DMD (±34° optical angle is available) with rectangular tip/tilt can benefit such a design. The quasi-confocal detection offered by the iris that filters unwanted light may find useful applications to separate light from guide stars at different depths of use in microscopy [27] and ophthalmology aided by the large dynamic range that may also benefit myopia [28] and highly-aberrated keratoconus studies and animal retinal imaging [29]. Finally, the DMD allows removal of unwanted light in the pupil plane such as reflections from the anterior eye in ophthalmology or bright stars in coronagraphy.

6. CONCLUSIONS

Quantification and correction of optical aberrations is essential in a wide range of fields. We have introduced a DMD-HS-WFS that uses raster scanning of the pupil with reflective DMD cells that probe a wavefront sequentially by sensing local tilts without the use of a lenslet array and thus without crosstalk. The sensor can potentially operate at kHz speed with few sampling points and switch to lower speed with denser sampling when required. We have provided a numerical analysis of the sensor and an experimental proof-of-principle.

Funding Information. H2020 ITN MyFUN (675137), UCD seed funding, and the King Abdullah scholarship program.

References

1. D. Malacara, *Optical Shop Testing* (Wiley, 2007).
2. J. Liang, B. Grimm, S. Goelz, and J. F. Bille, "Objective measurement of wave aberrations of the human eye with the use of a Hartmann-Shack wave-front sensor," J. Opt. Soc. Am. A **11**, 1949 (1994).
3. V. Akondi, C. Falldorf, S. Marcos, and B. Vohnsen, "Phase unwrapping with a virtual Hartmann-Shack wavefront sensor," Opt. Express **23**, 25425 (2015).
4. D. Valente, D. Rativa, and B. Vohnsen, "Wavefront sensing using a liquid-filled photonic crystal fiber," Opt. Express **23**, 13005 (2015).
5. F. Roddier, "Wavefront sensing and the irradiance transport equation," Appl. Opt. **29**, 1402 (1990).

6. R. Ragazzoni, "Pupil plane wavefront sensing with an oscillating prism," J. Mod. Opt. **43**, 289 (1996).
7. V. Akondi, S. Castillo, and B. Vohnsen, "Digital pyramid wavefront sensor with tunable modulation," Opt. Express **21**, 18261 (2013).
8. B. Vohnsen and D. Valente, "Surface-plasmon-based wavefront sensing," Optica **2**, 1024 (2015).
9. L. Seifert, J. Liesener, and H. J. Tiziani, "The adaptive Shack-Hartmann sensor," Opt. Commun. **216**, 313 (2003).
10. Y. Hongbin, Z. Guangya, C. F. Siong, L. Feiwen, and W. Shouhua, "A tunable Shack-Hartmann wavefront sensor based on a liquid-filled microlens array," J. Micromech. Microeng. **18**, 105017 (2008).
11. B. Lochocki, A. Gambín, S. Manzanera, E. Irles, E. Tajahuerce, J. Lancis, and P. Artal, "Single pixel camera ophthalmoscope," Optica **3**, 1056 (2016).
12. A. Carmichael Martins and B. Vohnsen, "Analysing the impact of myopia on the Stiles-Crawford effect of the first kind using a digital micromirror device," Ophthal. Physiol. Opt. (2018).
13. F. Soldevila, V. Durán, P. Clemente, J. Lancis, and E. Tajahuerce, "Phase imaging by spatial wavefront sampling," Optica **5**, 164 (2018).
14. H. Shinto, Y. Saita, and T. Nomura, "Shack–Hartmann wavefront sensor with large dynamic range by adaptive spot search method," Appl. Opt. **55**, 5413 (2016).
15. G. R. Brady, M. Guizar-Sicairos, and J. R. Fienup, "Optical wavefront measurement using phase retrieval with transverse translation diversity," Opt. Express **17**, 624 (2009).
16. L. N. Thibos, X. Hong, A. Bradley, and X. Cheng, "Statistical variation of aberration structure and image quality in a normal population of healthy eyes," J. Opt. Soc. Am. A **19**, 2329 (2002).
17. A. Roorda, F. Romero-Borja, W. J. Donnelly III, H. Queener, T. J. Hebert, and M. C.W. Campbell, "Adaptive optics scanning laser ophthalmoscopy," Opt. Express **10**, 405 (2002).
18. V. N. Mahajan and E. Acosta, "Vector polynomials for direct analysis of circular wavefront slope data," J. Opt. Soc. Am. A **34**, 1908 (2017).
19. L. Lundström and P. Unsbo, "Transformation of Zernike coefficients: scaled, translated, and rotated wavefronts with circular and elliptical pupils," J. Opt. Soc. Am. A **24**, 569 (2007).
20. R. Irwan and R. G. Lane, "Analysis of optimal centroid estimation applied to Shack–Hartmann sensing," Appl. Opt. **38**, 6737 (1999).
21. S. Thomas, T. Fusco, A. Tokovinin, M. Nicolle, V. Michau, and G. Rousset, "Comparison of centroid computation algorithms in a Shack-Hartmann sensor," Mon. Not. R. Astron. Soc. **371**, 323 (2006).
22. V. Akondi and B. Vohnsen, "Myopic aberrations: impact of centroiding noise in Hartmann Shack wavefront sensing," Ophthal. Physiol. Opt. **33**, 434 (2013).
23. S. Wang, P. Yang, B. Xu, L. Dong, and M. Ao, "Shack-Hartmann wavefront sensing based on binary-aberration-mode filtering," Opt. Express **23**, 5052 (2015).
24. M. Nicolle, T. Fusco, G. Rousset, and V. Michau, "Improvement of Shack-Hartmann wave-front sensor measurement for extreme adaptive optics," Opt. Lett. **29**, 2743 (2004).
25. M. Chen, F. S. Roux, and J. C. Olivier, "Detection of phase singularities with a Shack-Hartmann wavefront sensor," J. Opt. Soc. Am. A **24**, 1994 (2007).
26. A. Polo, F. Bociort, S.F. Pereira, H. P. Urbach, "Wavefront measurement for EUV lithography system through Hartmann sensor," Proc. SPIE **7971**, 79712R (2011).
27. A. R. Jewel, V. Akondi, B. Vohnsen, "A direct comparison between a MEMS deformable mirror and a liquid crystal spatial light modulator in signal-based wavefront sensing," J. Europ. Opt. Soc. **8**, 13073 (2013).
28. E. G. de la Cera, G. Rodríguez, L. Llorente, F. Schaeffel, and S. Marcos, "Optical aberrations in the mouse eye," Vision Res. **46**, 2546 (2006).
29. D. J. Wahl, Y. Jian, S. Bonora, R. J. Zawadzki, and M. V. Sarunic, "Wavefront sensorless adaptive optics fluorescence biomicroscope for in vivo retinal imaging in mice," Biomed. Opt. Express **7**, 1 (2016).